Optics Letters

Assessment of tight-binding models for high-harmonic generation in zinc blende materials

Miroslav Kolesik

James C. Wyant College of Optical Sciences, University of Arizona, Tucson, Arizona 85721, USA (kolesik@acms.arizona.edu)

Received 23 February 2023; revised 27 April 2023; accepted 5 May 2023; posted 8 May 2023; published 7 June 2023

Using a simulator for semiconductor Bloch equations (SBEs) accounting for the entire Brillouin zone, we examine the tight-binding (TB) description for zinc blende structure as a model for high-harmonic generation (HHG). We demonstrate that TB models of GaAs and ZnSe exhibit second-order nonlinear coefficients that compare favorably with measurements. For the higher-order portion of the spectrum, we use the results published by Xia *et al.* in Opt. Express 26, 29393 (2018) and show that the HHG spectra measured in reflection can be closely reproduced by our simulations free of adjustable parameters. We conclude that despite their relative simplicity, the TB models of GaAs and ZnSe represent useful tools to study both the low- and higher-order harmonic response in realistic simulations.

https://doi.org/10.1364/OL.488546

Numerical simulations play an important role in the field of high-harmonic generation in solids [1–3]. Given the challenges in front of the experiments and their interpretation, computer-aided modeling [4,5] offers much needed help in understanding various aspects of this extremely nonlinear, non-perturbative frequency-conversion process. In addition to *ab initio* calculations [6] and time-domain density functional theory [7,8], numerous works rely on the semiconductor Bloch equations [9–11]. Because of the sheer numerical complexity, approximations are often invoked to make the problem more manageable. For example, one frequently used approach consists of replacing the Brillouin zone with a one-dimensional "lineout" of Bloch states (e.g., [12,13]), which is orders of magnitude faster, but unable to fully capture the material symmetry. There are examples of (solid-state) high-harmonic generation (HHG) simulations which account for all microscopic states [14], but the price in terms of computing resources is high [7]. Consequently, most theory–experiment comparisons in the literature are qualitative in their nature.

As a step toward a more quantitative HHG modeling, we examine a class of tight-binding material models. While description based on first principles such as density functional theory (DFT) calculations are expected to be more accurate, their practical application, especially in the field of HHG, remains challenging. It therefore make sense to ask if simpler-to-use tight-binding models can be used for HHG simulation and if their simulated responses can be reasonably accurate across the whole spectrum. The main purpose of this work is to elevate the status of the tight-binding models in the HHG field from that of qualitative toy models to physically robust descriptions accurate enough to support *realistic simulations*.

Our first goal is to capture the high- and low-harmonic generation in a unified framework, and use the second harmonic for a comparison with experiments. More specifically, we test if the HHG models exhibit correct second-order nonlinear tensors, and if their simulated nonlinear coefficients (which is d_{14} for zinc blende structure) are comparable to their measured counterparts. Our results are encouraging, indicating that tight-binding descriptions are quite accurate in this respect. Next we use measurements on GaAs published by Xia *et al.* [15] and demonstrate that HHG spectra measured in the reflection geometry for different sample orientations can be closely reproduced by our simulations.

The enabling capability for this work is a recently developed HHG modeling method [16], which builds on the semiconductor Bloch equations (SBEs) [9–11] to simulate the material and the high-harmonic generation [4] excited by a non-resonant mid-infrared pulsed electric field $\mathbf{E}(t)$. With the details of the method given in Ref. [16], here we summarize its main features for the reader's convenience. The most important aspect of the algorithm is that the Bloch states from the entire Brillouin zone are all included in the simulation. This ensures that the induced current-density vector has the correct transformation properties reflecting the symmetry group of the material. Moreover, there is no degree of freedom to re-scale the strength of the simulated optical response. This makes it possible to test if the simulated nonlinearity compares well with the measured values.

To set the notation, let $\epsilon_n(\mathbf{k})$ with $n = 1, \ldots, N_b$ be the material energy bands. They are obtained by exact diagonalization of a tight-binding Hamiltonian $h(\mathbf{k})$ for each $\mathbf{k}$ from the Brillouin zone, producing the corresponding eigenvectors $\{|n\mathbf{k}\rangle\}$.

The density matrix $\rho_{mn}(\mathbf{k};t)$ evolves according to the SBE, which we represent in the time-dependent basis [17] $\{|n\mathbf{k}_t\rangle\}_n$ where the $\mathbf{k}$-vector $\mathbf{k}_t \equiv \mathbf{k} - \mathbf{A}(t)$ follows the vector potential $\mathbf{A}(t)$:

$$(i\partial_t - \epsilon_{nm}(\mathbf{k}_t))\rho_{nm}(\mathbf{k};t) = \mathbf{E}(t)\sum_a (\rho_{na}(\mathbf{k};t)\mathbf{d}_{am}(\mathbf{k}_t) - \mathbf{d}_{na}(\mathbf{k}_t)\rho_{am}(\mathbf{k};t)), \quad (1)$$

in which

$$\mathbf{d}_{nm}(\mathbf{k}_t) = \langle n\mathbf{k}_t | i\partial_{\mathbf{k}_t} | m\mathbf{k}_t\rangle \text{ and } \epsilon_{nm}(\mathbf{k}_t) = \epsilon_n(\mathbf{k}_t) - \epsilon_m(\mathbf{k}_t) \quad (2)$$

are the transition dipoles (for $m \neq n$) and Berry connections (for $m = n$), and the band-energy difference, respectively. Note that these equations require differentiability of $|n\mathbf{k}\rangle$ with respect to $\mathbf{k}$, which is called a smooth structure gauge [4].

The observable of interest is the current density obtained by integrating over the Brillouin zone and adding contributions from all bands [Eq. (62) in Ref. [17]],

$$\mathbf{j}(t) = \sum_{mn} \int \frac{d\mathbf{k}}{(2\pi)^3} \langle n\mathbf{k}_t | \partial_{\mathbf{k}_t} h(\mathbf{k}_t) | m\mathbf{k}_t \rangle \rho_{mn}(\mathbf{k}; t), \tag{3}$$

where $\partial_{\mathbf{k}} h(\mathbf{k})$ is the gradient of the Hamiltonian matrix. Since the analytic expression is at hand, it is straightforward to split the total current into inter- and intra-band contributions as it is often done. However, our comparisons with experiments do not require such a separation so it is not pursued.

Our method solves the above system via operator-splitting. Denoting by t_i the set of sampling times, and $\mathbf{k}_i = \mathbf{k} - \mathbf{A}(t_i)$, we obtain (by exact diagonalization) the eigensystem $\{\epsilon(\mathbf{k}_i), |a\mathbf{k}_i\rangle\}_{a=1}^{N_b}$ for the Hamiltonian at each t_i. The density-matrix evolution over the time step interval $\Delta t = t_{i+1} - t_i$ can be approximated by

$$\rho_{ab}(\mathbf{k}; t_{i+1}) = \sum_{uv} P^{(i)}_{au} \rho_{uv}(\mathbf{k}; t_i) (P^{(i)})^{\dagger}_{vb}, \tag{4}$$

where the evolution operator

$$P^{(i)}_{ab} = e^{-i\epsilon_a(\mathbf{k}_i)\frac{\Delta t}{2}} U^{(i)}_{ab} e^{-i\epsilon_a(\mathbf{k}_i)\frac{\Delta t}{2}} \quad \text{with} \quad U^{(i)}_{ab} = \langle a\mathbf{k}_{i+1} | b\mathbf{k}_i \rangle \tag{5}$$

encompasses the basis-transformation between $t_i \rightarrow t_{i+1}$, given by the unitary matrix $U^{(i)}_{ab}$. The scalar product required to evaluate elements of U is executed in the same basis the eigensystem solver is using so this calculation is inexpensive.

An integration step is completed by adding phenomenological dephasing to the off diagonal parts of the density matrix [4],

$$\rho_{ab} \rightarrow \rho_{ab} e^{-\Delta t/T_2} \quad \text{for} \quad a \neq b. \tag{6}$$

An important advantage of this algorithm is that dipole moments and/or the Berry connections [i.e., $\mathbf{d}_{nm}$ in Eq. (2)] are not needed, because all information concerning these quantities is encapsulated in $U^{(i)}_{ab}$. Moreover, the method works with arbitrary (even truly random) phases assigned to the eigenstates, and it is therefore completely free of the issues [18–20] related to the transition-dipole phases [21]. In particular, the construction of the smooth structure gauge [4] in not required.

We use this algorithm to examine the tight-binding description for the zinc blende structure as a tool to simulate high-harmonic generation. The tight-binding models are passed to the solver as a $\mathbf{k}$-dependent Hamiltonian $h(\mathbf{k})$ using the so-called sp^3s^* approximation [22,23]. We test the models with the inclusion of spin–orbit coupling (SOC), which give rise to 20-dimensional Hilbert spaces (i.e., 20 bands). The explicit form of $h(\mathbf{k})$ was taken from Ref. [24], and it was used to calculate the operator $\partial_{\mathbf{k}} h(\mathbf{k})$ required for the evaluation of the current-density, Eq. (3). The material-specific parameters were taken from [24], and we do not modify them in any way.

It is no secret among simulation practitioners that there are three parameters that can be adjusted to exercise significant control over how the simulated spectrum looks, namely: (i) the dephasing time T_2 may affect the peak-to-valley ratio; (ii) re-scaling of the material response controls the nonlinearity for the pulse propagation, which in turn changes the spectrum drastically; and iii) the intensity in the focus, which is often not known accurately, can influence the HHG cutoff. We emphasize that none of these parameters is used to "manipulate" the simulated spectrum to improve the agreement with the measured HHG spectra.

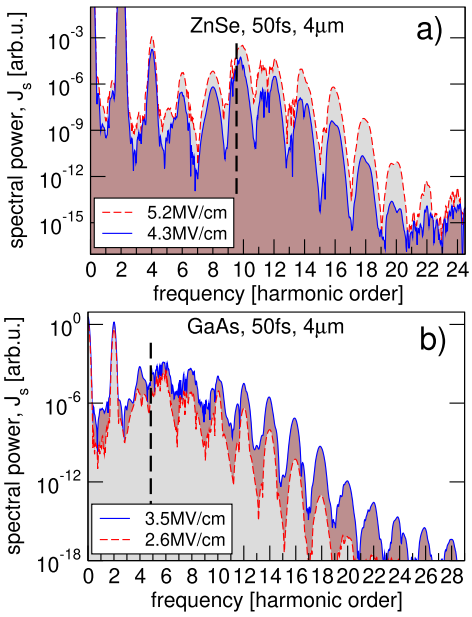

Fig. 1. (a), (b) Examples of HHG spectra for samples excited by a pulsed electric field oscillating along $(0, 1, 1)/\sqrt{2}$ (in crystal frame). The spectra of the s-polarized induced current density, J_s, only exhibit even harmonic orders. The dashed vertical lines mark the frequencies corresponding to bandgaps.

For our first numerical experiment, we assume that the material sample is excited by a pulsed electric field $\mathbf{E}(t)$ oscillating along the (110) crystal direction. The induced current density can be decomposed into parallel J_p and perpendicular J_s components. In this geometry, the crystal symmetry dictates that the second (and all even) harmonics appear in J_s. Figure 1 depicts examples of the J_s spectra simulated for GaAs and ZnSe with the SOC included and dephasing set to $T_2 = 50$ fs. The excitation pulse was a Gaussian with a 50-fs duration, and wavelength $\lambda = 4$ μm. Two not-too-different field amplitudes are chosen for each material to show that even a small field increment can cause very large changes in the spectral power, especially in the higher-frequency region. Our HHG spectra exhibit well-separated bands, and they do not change drastically for $T_2 = 100$ fs (not shown). Note that the weak sensitivity to T_2 is not a property specific to TB models. Rather, it is achieved by (i) the integration over the entire Brillouin zone and (ii) dense sampling ensuring proper convergence of the integral.

Continuing with the same setup and geometry, we examine the second harmonic (SH) but at much lower intensity, with $E_0 \approx 0.8$MV/cm for which we have checked that the SH power scales with the square of the fundamental intensity, indicating that the perturbative regime was reached. We have shown previously [16] that the simulations give the SH radiation patterns with correct symmetry properties. Here we aim to check if the corresponding nonlinear coefficients compare well with the measured values. For this purpose, we excite the material with a pulse and select the perpendicular component of the induced current, $J_s(t)$, which is dominated by the SH together with the rectified (near-zero frequency) radiation. To measure the nonlinear coefficient d_{14},

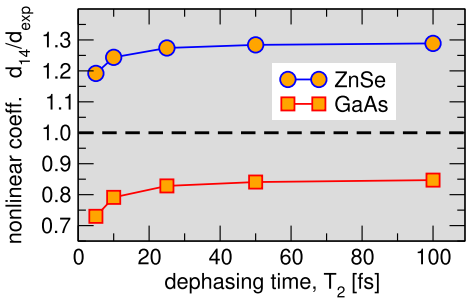

Fig. 2. Simulated nonlinear coefficient d_{14} as a function of the dephasing time for GaAs and ZnSe. Values are shown relative to those measured.

we band-pass the SH from $J_s(t)$, integrate over time to convert it to polarization, and use the relation for the SH specific for the zinc blende structure,

$$P_z(2\omega) = 2\epsilon_0 d_{14} E_x(\omega) E_y(\omega). \tag{7}$$

We repeat this procedure in simulations using different values of the dephasing time T_2 as this is the only parameter in our calculations that is not fixed. Note that d_{14} is a material property responding to the local field, so propagation effects do not enter in this numerical experiment. The results are shown in Fig. 2 for GaAs and for ZnSe. For the comparison with measured values, we use $d_{14} = 94$ pm/V from Ref. [25] for GaAs and 31 pm/V for ZnSe where the latter is obtained by Miller scaling from the value measured at 1.047 μm in Ref.@[26]. The figure depicts the simulated nonlinear coefficient in units of their experimental counterparts, so that the deviation from the dashed line can be interpreted as a measure of the relative error. We can see that for the longer dephasing times, the nonlinear coefficients stabilize at values which are within fifteen to fifty percent from their measured counterparts. Note that the experimental values themselves exhibit significant spread (see, e.g., [25]), especially at longer wavelengths, so this kind of gap between the simulated and experimental nonlinear coefficients is acceptable. It is encouraging that a rough agreement could be achieved without any adjustments to the material model.

Our results suggest that for short T_2, the second-order nonlinearity becomes weaker. Incidentally, very small T_2 values were preferred in a number of simulations reported in the literature (see discussions in [7] and [14]), because for longer T_2, the simulated harmonic bands tend to blur into a fine-structured supercontinuum which is not typical for experiments [1,15].

For the next test, we simulate some of the measurements from [15]. To avoid complications due to propagation effects, we concentrate on the high-harmonic spectra in reflection (RHHG) for two geometries. For setup A, we take a sample with 100 facets and pulse polarization at 45 degrees with respect to crystal axis. In setup B, the sample orientation is 011, and the electric polarization vector points at 45 degrees away from the x axis. As in the experiment, the excitation pulse with an electric field amplitude of 10 MV/cm (in the material) has the central wavelength of 3.5 μm and duration of 60 fs.

For a comparison with an experiment, it is necessary to take into account the Gaussian focal spot together with the fact that the spectrum is measured far from the sample. This is why we sample the beam profile at 15 radial points r_n (having checked

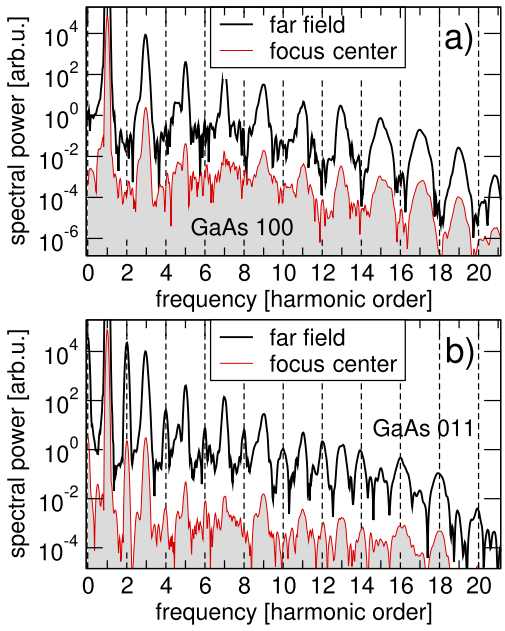

Fig. 3. Simulated RHHG spectra as observed far from the sample surface (thick black lines, see text for details of the far-field calculation) compared with the spectrum generated at the center of the focal spot. (a) Sample orientation 100 where the material symmetry prohibits even harmonic orders. (b) Sample orientation 011 where the response contains both even and odd harmonic orders.

with 30 that a convergence was achieved) evaluating the current response and its spectrum $S(\omega, r_n)$ at each. The far-field spectrum is obtained from the radial samples with the help of the discrete Hankel transform (DHT),

$$\hat{S}(\omega, k_m) = \sum_n H_{mn} S(\omega, r_n), \tag{8}$$

where both the radii r_n and transverse wavenumbers k_m are scaled zeros of the Bessel functions J_0, meaning $r_n = R\alpha_n$ and $k_n = \alpha_n/R$ with $J_0(\alpha_n) = 0$ and R standing for the transverse dimension of the computational domain large enough to accommodate the focal spot. Reference [27] gives an explicit expression for the transformation matrix H_{mn}. Because $k_0 > 0$, the true far-field spectrum on-axis, $\hat{S}(\omega, k_\perp = 0)$, is obtained by extrapolation from k_0 and k_1. This procedure is a realization of the so-called spatial filtering [28] in the reflection geometry where the sample surface acts as a distributed source of HHG. Linear polarization and sufficiently small numerical aperture is assumed for this calculation.

The far-field calculation, or spatial filtering [28], is important because it has two effects on the observed spectrum. By averaging over HHG realization driven by pulses with different peak amplitudes, the overall shape of the spectrum is affected. More importantly, the filtering cleans up fine structures present in the point spectra. Both these effects are illustrated in Fig. 3, comparing for both geometries the point spectrum corresponding to the center of the focal spot, and the resulting far-field spectrum. The far-field spectrum has less of the fine structure, and the peak-to-valley contrast is stronger.

Having calculated the far-field spectra, we are now ready for the most important result of this work, which is the comparison with the experiments by Xia *et al.* [15]. It should be emphasized

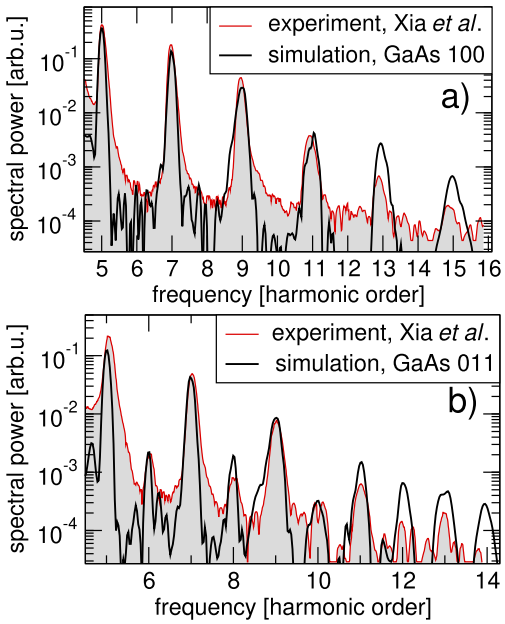

Fig. 4. Simulated HHG spectra (thick black line) compared with the measurement by Xia *et al.* [15] shown as gray-shaded area bounded by the thin red line. Panel (a) is for setup A, where symmetry forbids even-order generation. In contrast, all harmonic orders are symmetry-allowed in setup B shown in panel (b).

that there are no adjustable parameters that could change our simulation results; all GaAs model parameters are fixed, and the dephasing time T_2>50 fs has negligible influence because it is longer than the pulse. Among the experiment parameters, it is the peak amplitude inside the material that is hardest to estimate with accuracy, so some degree of adjustment would be permissible for this particular quantity, but for this work, we prefer to use the value given in [15] as is.

In Fig. 4, we compare our simulation results (including spatial averaging or far-field calculation) with the experimental RHHG spectra which we obtained by digitizing Figs. 2 and 6 of Ref. [15]. The figure excludes the region around the fourth harmonic because the experimental data contain a fluorescence peak. The agreement is very good and, in particular, the relative strength of the peaks is reproduced quite well for harmonics below order 12. The simulated harmonics 13 and higher do exhibit higher spectral power than the measurements, but given the extreme sensitivity with respect to the peak amplitude (see Fig. 1), the deviations are not unexpected. Importantly, our simulations faithfully reflect the material symmetry which shows up in the absence of even orders in Fig. 4(a) and in the relatively weaker even harmonic orders in Fig. 4(b).

We conclude that given the relative simplicity of the TB models, we have found a surprisingly favorable agreement with experiments in terms of the higher-order harmonic generation. The results show that, in applications related to HHG, the tight-binding models can be much more than qualitative toy models. The TB model performance demonstrated here should establish them as a tool to perform truly realistic HHG simulations. Since the GaAs and ZnSe models also exhibit nonlinear coefficients d_{14} which compare well with experiments, they can be useful for simulations involving frequency conversion in the below-bandgap region [29], and more generally for the modeling of mid-infrared laser materials [30].

Funding. DEVCOM Army Research Laboratory (W911NF1920192); Air Force Office of Scientific Research (FA9550-21-1-0463, FA9550-22-1-0182).

Disclosures. The authors declare no conflicts of interest.

Data availability. Data presented in this paper may be obtained from the authors upon reasonable request.

REFERENCES

1. S. Ghimire, A. D. DiChiara, E. Sistrunk, P. Agostini, L. F. DiMauro, and D. A. Reis, Nat. Phys. **7**, 138 (2011).
2. E. Goulielmakis and T. Brabec, Nat. Photonics **16**, 411 (2022).
3. J. Park, A. Subramani, S. Kim, and M. F. Ciappina, Adv. Phys.: X **7**, 2003244 (2022).
4. L. Yue and M. B. Gaarde, J. Opt. Soc. Am. B **39**, 535 (2022).
5. C. Yu, S. Jiang, and R. Lu, Adv. Phys.: X **4**, 1562982 (2019).
6. L. Plaja and L. Roso-Franco, Phys. Rev. B **45**, 8334 (1992).
7. I. Floss, C. Lemell, G. Wachter, V. Smejkal, S. A. Sato, X.-M. Tong, K. Yabana, and J. Burgdörfer, Phys. Rev. A **97**, 011401 (2018).
8. X.-Y. Wu, H. Liang, X.-S. Kong, Q. Gong, and L.-Y. Peng, Phys. Rev. E **105**, 055306 (2022).
9. M. Lindberg and S. W. Koch, Phys. Rev. B **38**, 3342 (1988).
10. H. Haug and S. W. Koch, *Quantum Theory of the Optical and Electronic Properties of Semiconductors* (World Scientific Publishing, 2009).
11. M. Kira and S. W. Koch, *Semiconductor Quantum Optics* (Cambridge University Press, 2011).
12. O. Schubert, M. Hohenleutner, F. Langer, B. Urbanek, C. Lange, U. Huttner, D. Golde, T. Meier, M. Kira, S. W. Koch, and R. Huber, Nat. Photonics **8**, 119 (2014).
13. I. Kilen, M. Kolesik, J. Hader, J. V. Moloney, U. Huttner, M. K. Hagen, and S. W. Koch, Phys. Rev. Lett. **125**, 083901 (2020).
14. G. G. Brown, A. Jiménez-Galán, R. E. F. Silva, and M. Ivanov, "A real-space perspective on dephasing in solid-state high harmonic generation," arXiv, arXiv:2210.16889 (2022).
15. P. Xia, C. Kim, F. Lu, T. Kanai, H. Akiyama, J. Itatani, and N. Ishii, Opt. Express **26**, 29393 (2018).
16. J. Gu and M. Kolesik, Phys. Rev. A **106**, 063516 (2022).
17. J. Wilhelm, P. Grössing, A. Seith, J. Crewse, M. Nitsch, L. Weigl, C. Schmid, and F. Evers, Phys. Rev. B **103**, 125419 (2021).
18. D. Wu, L. Li, Y. Zhan, T. Huang, H. Cui, J. Li, P. Lan, and P. Lu, Phys. Rev. A **105**, 063101 (2022).
19. S. Jiang, H. Wei, J. Chen, C. Yu, R. Lu, and C. D. Lin, Phys. Rev. A **96**, 053850 (2017).
20. S. Jiang, J. Chen, H. Wei, C. Yu, R. Lu, and C. D. Lin, Phys. Rev. Lett. **120**, 253201 (2018).
21. S. Jiang, C. Yu, J. Chen, Y. Huang, R. Lu, and C. D. Lin, Phys. Rev. B **102**, 155201 (2020).
22. P. Vogl, H. P. Hjalmarson, and J. D. Dow, J. Phys. Chem. Solids **44**, 365 (1983).
23. Ö. Akinci, H. H. Gürel, and H. Ülü, Thin Solid Films **517**, 2431 (2009).
24. A. D. Carlo, Semicond. Sci. Technol. **18**, R1 (2003).
25. T. Skauli, K. L. Vodopyanov, T. J. Pinguet, A. Schober, O. Levi, L. A. Eyres, M. M. Fejer, J. S. Harris, B. Gerard, L. Becouarn, E. Lallier, and G. Arisholm, Opt. Lett. **27**, 628 (2002).
26. H. P. Wagner, M. Kühnelt, W. Langbein, and J. M. Hvam, Phys. Rev. B **58**, 10494 (1998).
27. H. F. Johnson, Comp. Phys. Comm. **43**, 181 (1987).
28. C. Q. Abadie, M. Wu, and M. B. Gaarde, Opt. Lett. **43**, 5339 (2018).
29. S. Vasilyev, J. Gu, M. Mirov, Y. Barnakov, I. Moskalev, V. Smolski, J. Peppers, M. Kolesik, S. Mirov, and V. Gapontsev, J. Opt. Soc. Am. B **38**, 1625 (2021).
30. J. Gu, A. Schweinsberg, L. Vanderhoef, M. Tripepi, A. Valenzuela, C. Wolfe, T. R. Ensley, E. Chowdhury, and M. Kolesik, Opt. Express **29**, 7479 (2021).